Journal of Materials Chemistry A

ROYAL SOCIETY OF CHEMISTRY

PAPER

View Article Online
View Journal

Cite this: DOI: 10.1039/d1ta10433k

Aggregation of CeO_2 particles with aligned grains drives sintering of Pt single atoms in Pt/CeO_2 catalysts†

Jaeha Lee,‡[af] Sungsu Kang,‡[ab] Eunwon Lee,[a] Minho Kang,[ab] Jongbaek Sung,[ab] Tae Jin Kim,[e] Phillip Christopher,[f] Jungwon Park *[abcd] and Do Heui Kim *[a]

Understanding the sintering mechanism of platinum-group-metals (PGMs) supported on reducible oxides, such as CeO_2, is of fundamental and practical importance for the development of durable catalysts. It has been reported that the sintering of PGM nanoparticles occurs simultaneously with the aggregation of CeO_2 nanostructures during high temperature thermal treatment. However, mechanistic insights into the coupled sintering processes are insufficient, due to the lack of direct *in situ* observations of the atomic scale reconstruction processes. Here, we utilize *in situ* and *ex situ* transmission electron microscopy measurements to examine the processes of Pt and CeO_2 sintering in model catalytic materials consisting of Pt on isolated CeO_2 particles and Pt on aggregated CeO_2 particles with varying grain boundary alignment. CeO_2 particle aggregation is observed to occur most facilely at particle contacts with well aligned grain boundaries and in turn these contacts serve as locations of the most significant Pt sintering. Our results suggest that the surface reconstruction during CeO_2 aggregation provides the driving force for Pt sintering and provides new understanding of the sintering mechanism of PGM catalysts.

Received 6th December 2021
Accepted 8th February 2022

DOI: 10.1039/d1ta10433k

rsc.li/materials-a

Introduction

Platinum-group-metals (PGMs) on oxide supports serve as active sites in heterogeneous catalysts with applications ranging from three-way catalysts to oil refining.[1–8] The cost and scarcity of PGMs require that the metals should be finely dispersed on oxide supports to maximize metal utilization efficiency. CeO_2 is a widely used support material,[9] because PGM dispersions of 100% can be obtained on CeO_2.[4,10–32] However, CeO_2-supported PGMs suffer from sintering under reducing conditions at high temperature,[33,34] which can be detrimental to their catalytic activity. The sintering of Pt is often described by the enhanced mobility of Pt single atoms (SAs) resulting in the formation of Pt nanoparticles (NPs) at high temperature.[35–37] In addition, DFT calculations predict that hydroxylation of the CeO_2 surface promotes Pt mobility and sintering.[26] However, high-surface-area CeO_2 is also prone to severe aggregation at elevated temperatures (>600 °C, Fig. S1†), which can influence the mobility of supported Pt, and potentially, the sintering of Pt. Therefore, the mechanism of Pt sintering on CeO_2 surfaces must consider both Pt mobility and CeO_2 aggregation, and the microscopic origin of how these processes may be coupled.

The mobility of Pt SAs supported on reducible oxides has been mainly investigated by spectroscopic methods such as CO-Fourier-transform infrared (CO-FTIR) spectroscopy and X-ray absorption spectroscopy (XAS). While these techniques provide valuable information on Pt SAs, they are mainly focused on identifying the oxidation state or the coordination number of Pt. In addition, the inability of Pt SAs on the CeO_2 surface to bind CO probe molecules and the presence of a CeO_2 overlayer covering Pt NPs at high temperature further make it difficult to study how Pt sintering is spatially correlated with CeO_2 aggregation.[10,34]

Transmission electron microscopy (TEM) is an appropriate technique for examining the spatial correlation between Pt sintering and CeO_2 aggregation. Previous TEM observations demonstrate that the mobility and the sintering behavior of Pt SAs can depend on various factors, such as support materials and support surface facets, by simultaneously observing both the Pt SAs and Pt NPs.[29,38–40] However, possible changes in the

[a]School of Chemical and Biological Engineering, Institute of Chemical Processes, Seoul National University, Seoul 08826, Republic of Korea. E-mail: dohkim@snu.ac.kr; jungwonpark@snu.ac.kr

[b]Center for Nanoparticle Research, Institute for Basic Science (IBS), Seoul 08826, Republic of Korea

[c]Institute of Engineering Research, College of Engineering, Seoul National University, Seoul 08826, Republic of Korea

[d]Advanced Institutes of Convergence Technology, Seoul National University, 145, Gwanggyo-ro, Yeongtong-gu, Suwon-si, Gyeonggi-do, 16229, Republic of Korea

[e]Department of Materials Science and Chemical Engineering, Stony Brook University, Stony Brook, New York 11794, USA

[f]Department of Chemical Engineering, University of California Santa Barbara, Santa Barbara, California 93106, USA

† Electronic supplementary information (ESI) available. See DOI: 10.1039/d1ta10433k

‡ These authors contributed equally to this work.

surface structure of the CeO_2 support during catalysis and their effects on Pt sintering are still unclear. TEM observations of Pt/CeO_2 subjected to a high temperature pretreatment would unravel the spatial correlation between Pt sintering and CeO_2 aggregation, with the knowledge of the precise locations where Pt sintering and CeO_2 aggregation are initiated.

Here, we investigate the thermally driven restructuring of Pt/CeO_2 samples using atomically resolved TEM. Observations of Pt-containing (in the form of NPs and SAs) CeO_2 particles with controlled spatial separation (isolated and aggregated with varying grain boundary alignment) reveal that Pt sintering occurs primarily at the interface between aggregated CeO_2 particles, while Pt sintering is suppressed on isolated CeO_2 particles. In addition, we found that the degree of Pt sintering depends on the relative orientations of CeO_2 particles with respect to each other; Pt sintering primarily occurs at the interface of CeO_2 particles with grain boundaries in close alignment. It is hypothesized that reconstruction and diffusion of CeO_2 surfaces, which occur preferentially at well-aligned CeO_2 grain boundary interfaces, facilitate Pt mobility and provide the primary pathway for Pt sintering in aggregated CeO_2 support particles. This finding would provide useful information to understand the mobility of Pt SAs supported on the high-surface area CeO_2 support.

Experimental

Sample preparation

Pt was loaded on ceria (Rhodia, surface area, 135 $m^2\ g^{-1}$, average particle size, 8.5 nm) by the incipient wetness impregnation method with aqueous $Pt(NH_3)_4(NO_3)_2$ (Sigma-Aldrich, 99.99% grade, metal basis) solution as a metal precursor at room temperature. After impregnation, the samples were dried in an oven at 100 °C for 24 h. The dried samples were further treated by using 15 vol% O_2/N_2 or 10 vol% H_2/N_2 or N_2 at the selected temperature for 2 h. The oxidation at *X* °C, the reduction at *Y* °C or the N_2 treatment at *Z* °C are represented by *X*C, *Y*R and *Z*NC, respectively. For example, Pt/CeO_2 500C–250R–800NC was prepared by (i) oxidizing dried Pt/CeO_2 at 500 °C for 2 h, (ii) reducing Pt/CeO_2 500C at 250 °C for 2 h, and finally (iii) N_2 treating Pt/CeO_2 500C–250R at 800 °C for 2 h. The flow rate was always kept at 100 mL min^{-1}.

H_2-temperature programmed reduction (H_2-TPR)

The H_2-TPR curve was collected using a BEL-CAT-II (BEL Japan Inc.) equipped with a thermal conductivity detector. 0.05 g of the sample was pretreated under a 20 vol% O_2/Ar flow at 500 °C for 1 h. After cooling down to −90 °C under an Ar flow by using a cryo-device, the sample was exposed to 5 vol% H_2/Ar for 30 min to stabilize the TCD signal. Afterwards, the H_2-TPR curve was obtained by increasing the temperature from −90 to 900 °C with a ramping rate of 10 °C min^{-1}. The flow rate was 50 mL min^{-1}.

X-ray diffraction (XRD)

XRD patterns were obtained at a voltage of 40 kV and a current of 30 mA with Cu-Kα radiation ($\lambda = 0.1542$ nm) using a Mode 1 Smartlab diffractometer (Rigaku, Japan). A scanning-step size of 0.02° at a speed of 2.5° min^{-1} was used.

Raman spectroscopy

40 mg of Pt/CeO_2 was spread on a sample holder inside the environmental cell (LinkamCCR1000) to collect *in situ* Raman spectra. The spectra were collected with a Bay Spec Nomadic™ Raman spectrometer equipped with a confocal microscope (Olympus BX-51 upright microscope), volume phase gratings, and a dichroic filter. The sample was excited with a 532 nm laser. The scattered photons were focused onto a CCD detector (2048 × 64 pixels) with a spectral resolution of 4 cm^{-1}. After pretreatment at 350 °C in 3 vol% O_2/Ar for 30 min, Pt/CeO_2 was reduced by using 3 vol% H_2/Ar at 50 or 250 °C for 20 min. The Raman spectra were collected after cooling down the sample temperature to 50 °C under a He flow. The spectra were recorded by averaging 5 scans (100 s per scan). The flow rate was 30 mL min^{-1}.

Surface area measurement

N_2 adsorption/desorption isotherms were measured on a Micromeritics ASAP 2010 apparatus at a liquid N_2 temperature of −196 °C. Before analysis, all the catalysts were pretreated at 300 °C for 4 h under evacuation conditions.

Transmission electron microscopy

For high-angle annular dark-field (HAADF) scanning TEM (STEM) images and energy dispersive X-ray spectroscopy (EDS), powders of Pt/CeO_2 were diluted in ethanol and a drop of the sample solution was placed onto a lacey carbon TEM grid or a SiN_x TEM grid, which was subsequently dried under vacuum overnight at room temperature. All images were obtained using a JEM-ARM200F transmission electron microscope (JEOL, Japan) operated at 200 kV and installed at the National Center for Inter-University Research Facility in Seoul National University. The microscope was equipped with a spherical aberration corrector in the condenser lens (probe corrector). The convergence semi-angle was 19 mrad and the collection semi-angle spanned from 68 mrad to 280 mrad. For EDS, an Oxford Instruments X-Max SDD with an active area of 100 mm and a solid angle of 0.9 sr, equipped in the microscope was used. For *in situ* heating TEM of Pt/CeO_2 500C–250R, a JEM-2100F transmission electron microscope (JEOL) and a DENSsolutions Wildfire holder were used (see ESI Discussion II and Fig. S11 for details†).

Results and discussion

A model catalyst consisting of 2% by weight of Pt loaded on CeO_2 that was oxidized at 500 °C (500C treatment) was used for our analyses unless stated otherwise. With the starting hypothesis that CeO_2 sintering is a critical process coupled to Pt sintering, we started by identifying conditions that induce CeO_2 sintering using a combination of Raman spectroscopy and H_2 temperature programmed reduction (H_2-TPR).

The surface and bulk reduction of Pt/CeO_2 occurs in a H_2 environment below 250 °C and above 600 °C, respectively, as seen in the H_2-TPR curve (Fig. S2†).[41] The reduction of the surface of Pt/CeO_2 causes the cleavage of Pt–O–Ce bonds in addition to Ce–O bonds, as shown in the *in situ* Raman spectra (Fig. S3†).[42] To investigate the effect of Ce–O and Pt–O–Ce bond activation on CeO_2 sintering, we performed three types of thermal treatments on the Pt/CeO_2 500C sample: (i) 800C (oxidation at 800 °C), (ii) 800NC (N_2 treatment at 800 °C), and (iii) 250R → 800NC (reduction at 250 °C followed by N_2 treatment at 800 °C). (i) and (ii) represent the thermal treatment without the reductive activation of Ce–O or Pt–O–Ce bonds, while (iii) is the thermal treatment following the reductive activation of Ce–O or Pt–O–Ce bonds. The average crystallite size of CeO_2 in Pt/CeO_2, estimated from XRD, increases from 8.6 to 9.8 nm both after (i) 800C and (ii) 800NC treatments, while it increases to 31.1 nm after (iii) (Fig. 1a). These results clearly indicate that the crystallite size of CeO_2 in Pt/CeO_2 becomes larger after high temperature treatment following reductive activation of Ce–O or Pt–O–Ce bonds. It should be noted that the crystallite sizes of Pt-free CeO_2 particles, measured from XRD, after the three types of the thermal treatment are similar to 17.2 nm (Fig. S4†). This is because thermal energy at 250 °C is insufficient to activate Ce–O bonds on CeO_2; the surface reduction of CeO_2 can occur below 250 °C in the presence of Pt (Fig. S2†).

The effect of various high-temperature treatments on the sizes of CeO_2 particles and Pt species in Pt/CeO_2 was studied by HAADF-STEM. CeO_2 particles smaller than 10 nm are observed in Pt/CeO_2 500C–250R (Fig. 1b and c), while CeO_2 particles larger than 30 nm are observed in Pt/CeO_2 500C–250R–800NC (Fig. 1e and f), consistent with the XRD measurements. On the other hand, abundant Pt SAs, along with Pt clusters as small as 1 nm are observed in Pt/CeO_2 500C–250R (Fig. 1c, d and S5†), while many Pt NPs larger than 1 nm and fewer Pt SAs are observed in Pt/CeO_2 500C–250R–800NC (Fig. 1e–g and S6–S8†). These results demonstrate that high-temperature treatment at 800 °C induces Pt sintering as well as CeO_2 aggregation on Pt/CeO_2 500C–250R.

These results are consistent with the recent study by Alcala *et al.*, where they suggested that the presence of Pt and other transition metal SAs reduces the surface mobility of CeO_2, helping to slow CeO_2 aggregation.[43] Once the Pt atoms become mobile on a CeO_2 surface through the activation of Pt–O–Ce bonds, the mobility of surface Ce atoms will subsequently be enhanced, leading to CeO_2 aggregation. However, the other scenario is also possible that the mobility of Pt SAs can be enhanced by the movements of surface atoms in CeO_2 during the process of CeO_2 aggregation. Investigating the casual relationship between the two situations – (i) CeO_2 aggregation promoted by Pt sintering and (ii) Pt sintering promoted by CeO_2 aggregation – is challenging because Pt sintering and CeO_2 aggregation occur simultaneously. This requires controlling the extent of CeO_2 aggregation, which can be accomplished by adjusting the interparticle distances of CeO_2 particles.

We analyzed the progress of Pt sintering that occurs at high temperatures *via in situ* and *ex situ* (S)TEM of the samples in which the interparticle distances of CeO_2 are controlled. We prepared Pt/CeO_2 particles on silicon nitride (SiN_x) TEM grids at low particle densities to deposit Pt/CeO_2 particles with diverse interparticle distances in a field of view. The SiN_x TEM grid plays dual roles as a thermally stable substrate for the high-

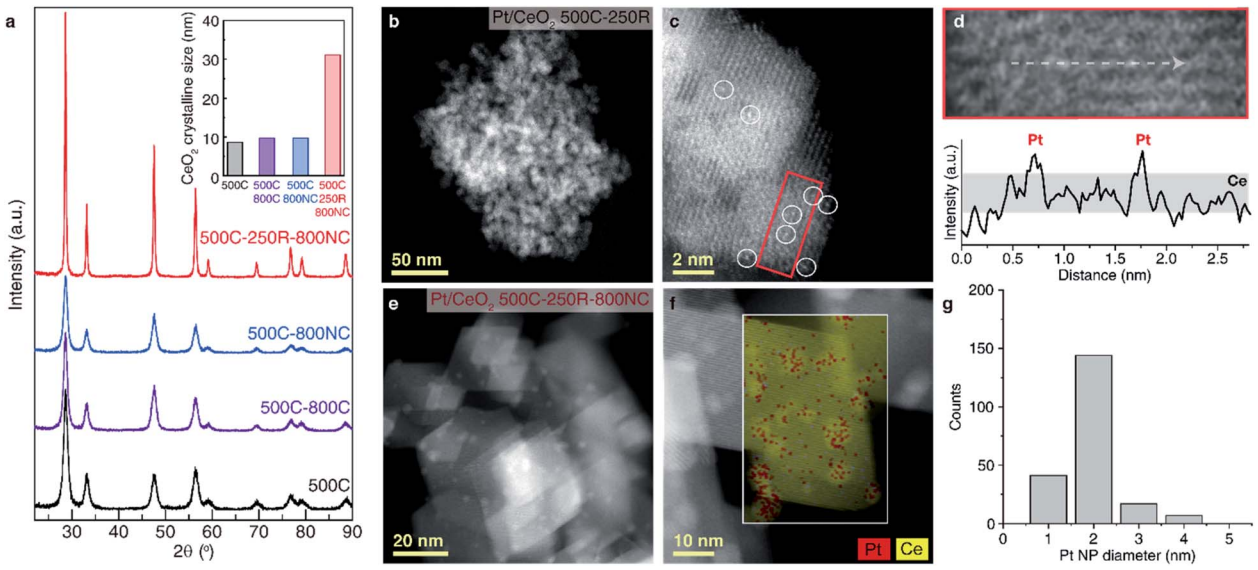

Fig. 1 CeO_2 aggregation and Pt sintering of surface-reduced Pt/CeO_2. (a) XRD patterns of Pt/CeO_2 500C (black), 500C–800C (purple), 500C–800NC (blue), and 500C–250R–800NC (red), and CeO_2 crystallite sizes of the corresponding samples calculated by using the Scherrer equation (inset). (b and c) Low-magnification (b) and high-resolution (c) HAADF-STEM image of Pt/CeO_2 500C–250R. (d) Low-pass filtered, magnified view of the region marked in (c) (upper panel) and the intensity profile along the line (lower panel). (e and f) HAADF-STEM image of Pt/CeO_2 500C–250R–800NC (e), and EDS elemental maps of Pt and Ce (f). (g) Histogram showing the diameter of Pt NPs in Pt/CeO_2 500C–250R–800NC.

temperature treatment and an electron-transparent window for direct, high-resolution (S)TEM without further handling (Fig. S9 and ESI Discussion I†). While controlling the interparticle distances of CeO_2 particles would be difficult for powder samples, we could make the variations in the interparticle distances by dispersing the samples on the TEM grids.

When Pt/CeO_2 500C–250R is dispersed on a SiN_x TEM grid and subsequently 800NC-treated, regions with densely packed CeO_2 particles and sparsely distributed CeO_2 particles are randomly formed (Fig. 2a). After 800NC treatment, CeO_2 aggregation and Pt sintering occur simultaneously in regions with high initial density of CeO_2 particles (Fig. 2b and c), with more significant particle growth occurring in the more aggregated areas; Fig. 2c compared to 2b. Alternatively, CeO_2 aggregation and Pt sintering are suppressed in regions with low initial density of CeO_2 particles (Fig. 2d). For example, isolated Pt/CeO_2 particles maintain their initial size of ~10 nm without aggregation during 800NC treatment (Fig. 2d). Furthermore, Pt SAs with high concentrations are clearly observed in the HAADF-STEM images of the isolated Pt/CeO_2 particles (Fig. 2e, f and S10†). If Pt sintering had occurred irrespective of CeO_2 aggregation, then Pt sintering should have occurred even on the isolated CeO_2 particles. Therefore, the observation of the maintained existence of Pt SAs on isolated CeO_2 particles, and significant Pt sintering in aggregated CeO_2 particles, demonstrates that thermal energy alone is not sufficient to drive Pt sintering and instead that Pt sintering is coupled to CeO_2 aggregation.

The mechanism of how CeO_2 aggregation induces Pt sintering was investigated by *in situ* heating TEM of Pt/CeO_2 500C–250R (Fig. S11, S12 and ESI Discussion II†). Pt/CeO_2 particles are dispersed with random orientations on a SiN_x grid at 600 °C (Fig. 3a). As the temperature increases further, CeO_2 particles rotate, and grain growth begins to occur, as evidenced by the temperature dependent appearance of lattice fringes in the *in situ* TEM images and the CeO_2 (111) peaks in fast-Fourier transforms (FFT) of the images (Fig. 3a and b). The rotation of crystalline NPs before aggregation is considered energetically favorable, as it can preclude the formation of grain boundaries with high mismatch and interfacial energy.[44–46] Grain boundaries with better orientations between the grains provide lower energy pathways for the diffusion of Ce and O atoms on the nanocrystal surfaces, which are required for the reconstruction and densification of aggregated CeO_2 particles.[46–48] Significant Ce and O diffusion, along with CeO_2 surface reconstruction, must accompany the aggregation of irregularly shaped CeO_2 particles (Fig. 2d). Notably, *in situ* heating TEM (Fig. 3a) and following STEM (Fig. 3b) clearly confirm that the formation of Pt NPs by Pt sintering at an elevated temperature progresses along with the aggregation of CeO_2 particles.

The sintering behavior of Pt atoms depending on the relative orientation of CeO_2 particles can be further investigated by observing the Pt/CeO_2 particles dispersed on a substrate with an appropriate density. Under these conditions the relative orientation of the grains of individual CeO_2 particles at interfacial junctions can be resolved by HAADF-STEM after 800NC treatment (Fig. 3c). On examining a grain boundary with a significantly mismatched angle of ~53° between (02$\bar{2}$) planes of contacting CeO_2 particles (Fig. 3d), abundant Pt SAs are found (Fig. 3e and f). On the other hand, in a grain boundary with a small mismatch angle of ~12° between (111) planes of contacting CeO_2 particles (Fig. 3g), individual Pt SAs cannot be clearly identified (Fig. 3h). Instead, Pt NPs are observed at the edge of the grain boundary of aggregating CeO_2 particles (Fig. 3g). This indicates that the mobility of Pt SAs increases during the aggregation of relatively well-aligned CeO_2 particles,

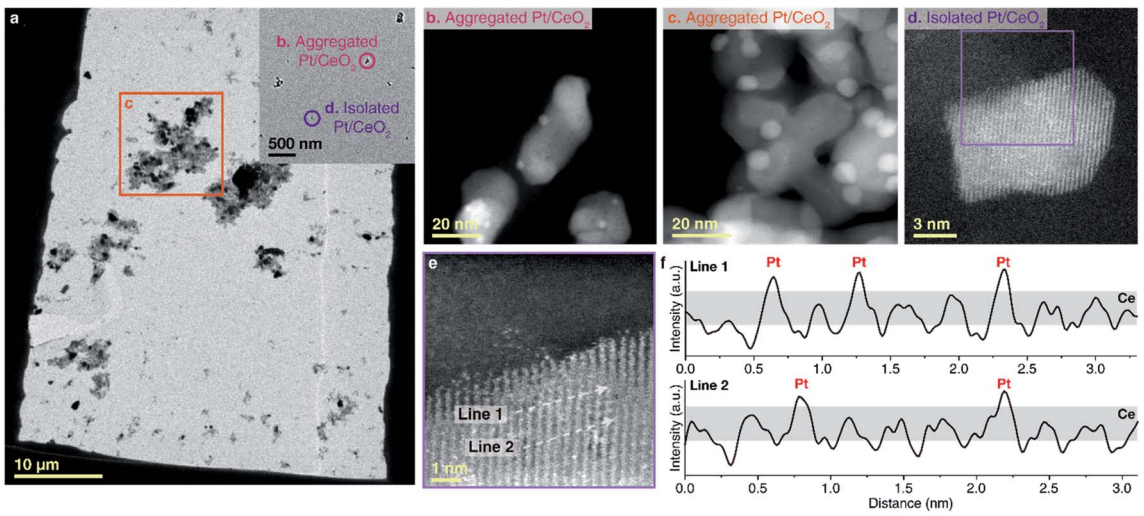

Fig. 2 Pt sintering induced by CeO_2 aggregation. (a) TEM image showing a SiN_x TEM grid after 800NC treatment of Pt/CeO_2 500C–250R. (Inset) TEM image showing mildly aggregated Pt/CeO_2 particles and isolated Pt/CeO_2 particles on the SiN_x TEM grid. (b–d) HAADF-STEM images of mildly aggregated Pt/CeO_2 particles (b), severely aggregated Pt/CeO_2 particles (c), and an isolated Pt/CeO_2 particle (d). Each image is taken at the region annotated in (a). (e) Low-pass filtered, enlarged image of the region marked in (d). (f) Intensity profiles along the lines shown in (e), showing the presence of Pt SAs on the isolated Pt/CeO_2 particle.

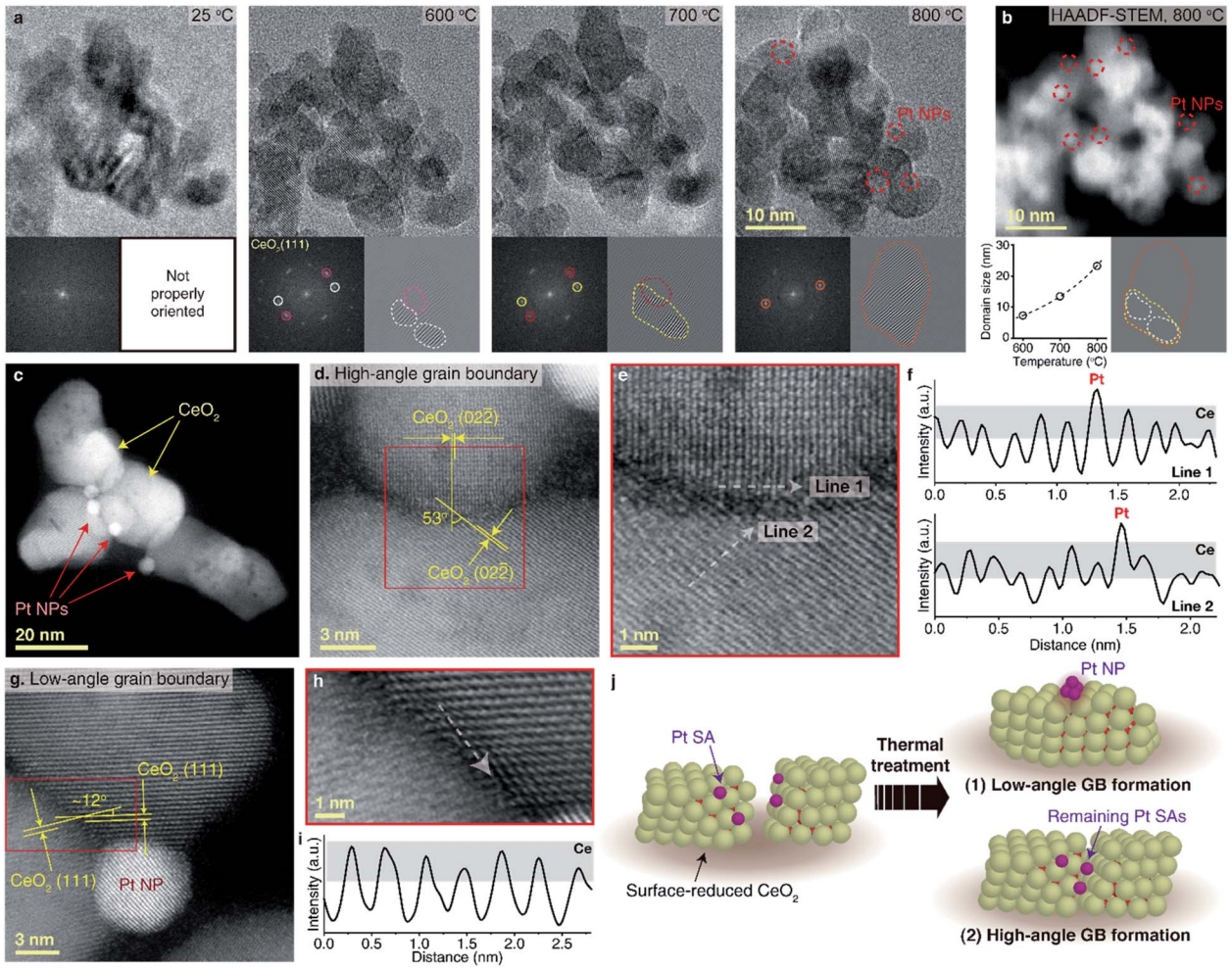

Fig. 3 Pt sintering driven by CeO_2 surface reconstruction. (a) TEM images of Pt/CeO_2 500C–250R during *in situ* heating (upper panels), corresponding FFTs (lower left panels), and inverse FFTs showing CeO_2 (111) domains selected from the FFTs (lower right panels). (b) HAADF-STEM image of Pt/CeO_2 500C–250R at 800 °C (upper panel), and the changes in average CeO_2 (111) domain sizes (lower left panel), measured from time-lapse inverse FFTs shown in (a) (lower right panel). (c) HAADF-STEM image of mildly aggregated Pt/CeO_2 on a SiN_x TEM grid. (d) HAADF-STEM images of CeO_2 particles forming a high-angle grain boundary. (e) The enlarged image of the marked region in (d). (f) Intensity profiles along the lines marked in (e). (g) HAADF-STEM images of CeO_2 particles forming a low-angle grain boundary. (h) The enlarged image of the marked region in (h). (i) Intensity profiles along the line marked in (h). (j) Scheme illustrating the sintering process. (1) When the neighboring lattice-aligned CeO_2 particles aggregate, Pt sintering occurs together with surface reconstruction. (2) The migration of Pt is suppressed when the neighboring CeO_2 particles are in contact with a high-angle grain boundary.

where surface reconstruction through surface diffusion of Ce and O species is kinetically more facile than in boundaries between mismatched grains.

As discussed previously, CeO_2 aggregation must accompany the surface reconstruction of CeO_2 particles, because (i) the O atoms on the O-terminated CeO_2 surface should be removed for the densification of the aggregating CeO_2 particles and (ii) each of the CeO_2 particles before aggregation is irregularly shaped (Fig. 2d) so that they can change their shape to aggregate to larger particles. During the surface reconstruction of CeO_2, Pt is likely to obtain mobility and eventually sinter into the larger particle at the edge of the aggregating particles ((1) in Fig. 3j). On the other hand, for CeO_2 particles with high misorientation angles, more energy would be required to align the particles, and therefore, the reconstruction of the interface and the diffusion of Pt SAs would be hindered ((2) in Fig. 3j).

We conducted additional experiments to investigate if CeO_2 aggregation can promote Pt sintering at a lower temperature. XRD patterns show that aggregation of CeO_2 particles into the larger crystals marginally occurs by 500NC treatment (Fig. S13†), while sintered Pt is observed in HAADF-STEM (Fig. S14†). Interestingly, HAADF-STEM shows the alignment of CeO_2 lattices and the partial aggregation of the neighboring CeO_2 particles (Fig. S14†). This indicates that even the partial aggregation of CeO_2 particles by lattice alignment at a low temperature may provide a sufficient driving force for Pt sintering.

Although the simultaneous occurrence of Pt sintering and CeO_2 aggregation is confirmed with both bulk characterization (XRD) and microscopic characterization (TEM), it should be noted that the promotion of Pt sintering by CeO_2 aggregation could be identified only with TEM. Thus, we have mainly

focused on TEM characterization that can unravel the spatial correlation between Pt sintering and CeO_2 aggregation. While we observed this correlation in multiple regions of the sample with TEM to give statistical meaningfulness to our finding, the evidences from bulk characterization tools will further supplement our understanding of the correlation between Pt sintering and CeO_2 aggregation. In this study, CeO_2 from Rhodia is used. The observed event, promoting Pt sintering by CeO_2 aggregation, presumably occurs universally on a CeO_2 support, regardless of its source or the synthesis method, because aggregation of CeO_2 with a high surface area commonly occurs at high temperature.

While the sintering of Pt SA on the CeO_2 surface has been studied for decades, it should be emphasized that the effect of CeO_2 aggregation on Pt sintering has not been fully understood. This would partly originate from the different models used to study Pt/CeO_2. For example, in most DFT models of Pt/CeO_2 or model Pt/CeO_2 systems in surface science, CeO_2 aggregation does not occur because the CeO_2 surface is infinitely expanded or the CeO_2 particles are spatially isolated. However, in high-surface-area powder samples, high temperature treatment would promote CeO_2 aggregation. Therefore, we believe that understanding how CeO_2 aggregation in high-surface-area powder samples promotes Pt sintering would be vital to develop thermally stable SA catalysts.

Conclusions

In this work, we show that the aggregation of the catalyst support, CeO_2, can induce the sintering of Pt atoms supported on surface-reduced CeO_2 particles. XRD and TEM show that Pt sintering and CeO_2 aggregation occur simultaneously. In order to unravel how CeO_2 aggregation influences Pt sintering, the extent of CeO_2 aggregation was controlled by changing the interparticle distance of CeO_2 particles by dispersing them on TEM grids. TEM of Pt/CeO_2 particles with different extents of CeO_2 aggregation shows that Pt sintering is promoted in the regions with severe CeO_2 aggregation, while abundant Pt SAs are found on spatially isolated CeO_2 particles where their aggregation is suppressed even at 800 °C. In addition, *in situ* TEM and high-resolution TEM indicate that Pt sintering is promoted at the low-angle grain boundary, indicating that the surface reconstruction of CeO_2 supports during their aggregation facilitates the migration of Pt SAs and Pt sintering. Our results uncover the unexplored sintering mechanism of supported Pt catalysts which should be considered to develop thermally stable catalysts with the high metal dispersion.

Author contributions

J. L. and D. H. K. designed the research. J. L. and E. L. synthesized and characterized the Pt/CeO_2 catalysts. S. K. conducted the STEM experiments. J. L., S. K., M. K., and J. S. performed *in situ* TEM. J. L. and S. K. performed analysis and interpretation of experimental results. J. L. and T. J. K. performed *in situ* Raman spectroscopy. P. C., J. P., and D. H. K. supervised the research effort. All the authors contributed to the writing of the manuscript and to the discussion of the results.

Conflicts of interest

There are no conflicts to declare.

Acknowledgements

This work was supported by the National Research Foundation of Korea (NRF) grant funded by the Korean Government (MSIT) (NRF-2016R1A5A1009592) (D. H. K.) (NRF-2019M3E6A1064877 and NRF-2021M3H4A1A02049904) (J. P.); the Institute for Basic Science (IBS-R006-D1) (J. P.); the Science Research Center (NRF-2017R1A5A1015365) (J. P.). This work was also supported by a Postdoctoral Fellowship program granted by NRF (2020R1A6A3A03039683) (J. L.).

Notes and references

1 Q.-A. Huang, A. Haruta, Y. Kumamoto, H. Murayama, E. Yamamoto, T. Honma, M. Okumura, H. Nobutou and M. Tokunaga, *Appl. Catal., B*, 2021, **296**, 120333.
2 S. Yoon, H. Ha, J. Kim, E. Nam, M. Yoo, B. Jeong, H. Y. Kim and K. An, *J. Mater. Chem. A*, 2021, **9**, 26381–26390.
3 D.-Y. Wei, M.-F. Yue, S.-N. Qin, S. Zhang, Y.-F. Wu, G.-Y. Xu, H. Zhang, Z.-Q. Tian and J.-F. Li, *J. Am. Chem. Soc.*, 2021, **143**, 15635–15643.
4 S. Zhang, L. Chen, Z. Qi, L. Zhuo, J.-L. Chen, C.-W. Pao, J. Su and G. A. Somorjai, *J. Am. Chem. Soc.*, 2020, **142**, 16533–16537.
5 J. L. Vincent and P. A. Crozier, *Nat. Commun.*, 2021, **12**, 5789.
6 J. Zhang, D. Zhu, J. Yan and C.-A. Wang, *Nat. Commun.*, 2021, **12**, 6665.
7 J. Ke, W. Zhu, Y. Jiang, R. Si, Y.-J. Wang, S.-C. Li, C. Jin, H. Liu, W.-G. Song, C.-H. Yan and Y.-W. Zhang, *ACS Catal.*, 2015, **5**, 5164–5173.
8 K. Khivantsev, C. G. Vargas, J. Tian, L. Kovarik, N. R. Jaegers, J. Szanyi and Y. Wang, *Angew. Chem., Int. Ed.*, 2021, **60**, 391–398.
9 A. Trovarelli, *Catal. Rev.*, 1996, **38**, 439–520.
10 J. Resasco, L. DeRita, S. Dai, J. P. Chada, M. Xu, X. Yan, J. Finzel, S. Hanukovich, A. S. Hoffman, G. W. Graham, S. R. Bare, X. Pan and P. Christopher, *J. Am. Chem. Soc.*, 2020, **142**, 169–184.
11 Y. Lu, S. Zhou, C.-T. Kuo, D. Kunwar, C. Thompson, A. S. Hoffman, A. Boubnov, S. Lin, A. K. Datye, H. Guo and A. M. Karim, *ACS Catal.*, 2021, **11**, 8701–8715.
12 Y. Ma, B. Chi, W. Liu, L. Cao, Y. Lin, X. Zhang, X. Ye, S. Wei and J. Lu, *ACS Catal.*, 2019, **9**, 8404–8412.
13 F. Maurer, J. Jelic, J. Wang, A. Gänzler, P. Dolcet, C. Wöll, Y. Wang, F. Studt, M. Casapu and J.-D. Grunwaldt, *Nat. Catal.*, 2020, **3**, 824–833.
14 X. I. Pereira-Hernández, A. DeLaRiva, V. Muravev, D. Kunwar, H. Xiong, B. Sudduth, M. Engelhard, L. Kovarik, E. J. M. Hensen, Y. Wang and A. K. Datye, *Nat. Commun.*, 2019, **10**, 1358.

15 Z. Qi, L. Chen, S. Zhang, J. Su and G. A. Somorjai, *J. Am. Chem. Soc.*, 2021, **143**, 60–64.
16 B. Song, D. Choi, Y. Xin, C. R. Bowers and H. Hagelin-Weaver, *Angew. Chem., Int. Ed.*, 2021, **60**, 4038–4042.
17 Z. Sun, S. Wang and W. Chen, *J. Mater. Chem. A*, 2021, **9**, 5296–5319.
18 C. Wang, X.-K. Gu, H. Yan, Y. Lin, J. Li, D. Liu, W.-X. Li and J. Lu, *ACS Catal.*, 2017, **7**, 887–891.
19 H. Wang, J.-X. Liu, L. F. Allard, S. Lee, J. Liu, H. Li, J. Wang, J. Wang, S. H. Oh, W. Li, M. Flytzani-Stephanopoulos, M. Shen, B. R. Goldsmith and M. Yang, *Nat. Commun.*, 2019, **10**, 3808.
20 X. Wang, J. A. van Bokhoven and D. Palagin, *Phys. Chem. Chem. Phys.*, 2020, **22**, 28–38.
21 A. Beniya and S. Higashi, *Nat. Catal.*, 2019, **2**, 590–602.
22 Y. Xiao, H. Li and K. Xie, *Angew. Chem., Int. Ed.*, 2021, **60**, 5240–5244.
23 H. Wang, M. Kottwitz, N. Rui, S. D. Senanayake, N. Marinkovic, Y. Li, R. G. Nuzzo and A. I. Frenkel, *ACS Appl. Mater. Interfaces*, 2021, **13**, 52736–52742.
24 H. Xiong, D. Kunwar, D. Jiang, C. E. García-Vargas, H. Li, C. Du, G. Canning, X. I. Pereira-Hernandez, Q. Wan, S. Lin, S. C. Purdy, J. T. Miller, K. Leung, S. S. Chou, H. H. Brongersma, R. ter Veen, J. Huang, H. Guo, Y. Wang and A. K. Datye, *Nat. Catal.*, 2021, **4**, 830–839.
25 M. Hatanaka, N. Takahashi, T. Tanabe, Y. Nagai, K. Dohmae, Y. Aoki, T. Yoshida and H. Shinjoh, *Appl. Catal., B*, 2010, **99**, 336–342.
26 A. Bruix, Y. Lykhach, I. Matolínová, A. Neitzel, T. Skála, N. Tsud, M. Vorokhta, V. Stetsovych, K. Ševčíková, J. Mysliveček, R. Fiala, M. Václavů, K. C. Prince, S. Bruyère, V. Potin, F. Illas, V. Matolín, J. Libuda and K. M. Neyman, *Angew. Chem., Int. Ed.*, 2014, **53**, 10525–10530.
27 N. Daelman, M. Capdevila-Cortada and N. López, *Nat. Mater.*, 2019, **18**, 1215–1221.
28 H. Jeong, G. Lee, B.-S. Kim, J. Bae, J. W. Han and H. Lee, *J. Am. Chem. Soc.*, 2018, **140**, 9558–9565.
29 J. Jones, H. Xiong, A. T. DeLaRiva, E. J. Peterson, H. Pham, S. R. Challa, G. Qi, S. Oh, M. H. Wiebenga, X. I. Pereira Hernández, Y. Wang and A. K. Datye, *Science*, 2016, **353**, 150–154.
30 M. Kottwitz, Y. Li, R. M. Palomino, Z. Liu, G. Wang, Q. Wu, J. Huang, J. Timoshenko, S. D. Senanayake, M. Balasubramanian, D. Lu, R. G. Nuzzo and A. I. Frenkel, *ACS Catal.*, 2019, **9**, 8738–8748.
31 D. Kunwar, C. Carrillo, H. Xiong, E. Peterson, A. DeLaRiva, A. Ghosh, G. Qi, M. Yang, M. Wiebenga, S. Oh, W. Li and A. K. Datye, *Appl. Catal., B*, 2020, **266**, 118598.
32 D. Kunwar, S. Zhou, A. DeLaRiva, E. J. Peterson, H. Xiong, X. I. Pereira-Hernández, S. C. Purdy, R. ter Veen, H. H. Brongersma, J. T. Miller, H. Hashiguchi, L. Kovarik, S. Lin, H. Guo, Y. Wang and A. K. Datye, *ACS Catal.*, 2019, **9**, 3978–3990.
33 Y. Nagai, T. Hirabayashi, K. Dohmae, N. Takagi, T. Minami, H. Shinjoh and S. Matsumoto, *J. Catal.*, 2006, **242**, 103–109.
34 J. Lee, C. Li, S. Kang, J. Park, J. M. Kim and D. H. Kim, *J. Catal.*, 2021, **395**, 246–257.
35 T. W. Hansen, A. T. DeLaRiva, S. R. Challa and A. K. Datye, *Acc. Chem. Res.*, 2013, **46**, 1720–1730.
36 E. D. Goodman, J. A. Schwalbe and M. Cargnello, *ACS Catal.*, 2017, **7**, 7156–7173.
37 E. D. Goodman, A. C. Johnston-Peck, E. M. Dietze, C. J. Wrasman, A. S. Hoffman, F. Abild-Pedersen, S. R. Bare, P. N. Plessow and M. Cargnello, *Nat. Catal.*, 2019, **2**, 748–755.
38 L. DeRita, J. Resasco, S. Dai, A. Boubnov, H. V. Thang, A. S. Hoffman, I. Ro, G. W. Graham, S. R. Bare, G. Pacchioni, X. Pan and P. Christopher, *Nat. Mater.*, 2019, **18**, 746–751.
39 R. Alcala, A. DeLaRiva, E. J. Peterson, A. Benavidez, C. E. Garcia-Vargas, D. Jiang, X. I. Pereira-Hernández, H. H. Brongersma, R. ter Veen, J. Staněk, J. T. Miller, Y. Wang and A. Datye, *Appl. Catal., B*, 2020, **284**, 119722.
40 Y. Li, M. Kottwitz, J. L. Vincent, M. J. Enright, Z. Liu, L. Zhang, J. Huang, S. D. Senanayake, W.-C. D. Yang, P. A. Crozier, R. G. Nuzzo and A. I. Frenkel, *Nat. Commun.*, 2021, **12**, 914.
41 J. Lee, Y. Ryou, X. Chan, T. J. Kim and D. H. Kim, *J. Phys. Chem. C*, 2016, **120**, 25870–25879.
42 M. S. Brogan, T. J. Dines and J. A. Cairns, *J. Chem. Soc., Faraday Trans.*, 1994, **90**, 1461–1466.
43 R. Alcala, A. DeLaRiva, E. J. Peterson, A. Benavidez, C. E. Garcia-Vargas, D. Jiang, X. I. Pereira-Hernández, H. H. Brongersma, R. ter Veen, J. Staněk, J. T. Miller, Y. Wang and A. Datye, *Appl. Catal., B*, 2021, **284**, 119722.
44 R. Theissmann, M. Fendrich, R. Zinetullin, G. Guenther, G. Schierning and D. E. Wolf, *Phys. Rev. B*, 2008, **78**, 205413.
45 D. Li, M. H. Nielsen, J. R. I. Lee, C. Frandsen, J. F. Banfield and J. J. De Yoreo, *Science*, 2012, **336**, 1014–1018.
46 G. Gottstein, *Physical Foundations of Materials Science*, Springer Berlin Heidelberg, Berlin, Heidelberg, 2004.
47 G. I. Nkou Bouala, N. Clavier, S. Martin, J. Léchelle, J. Favrichon, H. P. Brau, N. Dacheux and R. Podor, *J. Phys. Chem. C*, 2016, **120**, 386–395.
48 F. Polo-Garzon, Z. Bao, X. Zhang, W. Huang and Z. Wu, *ACS Catal.*, 2019, **9**, 5692–5707.